CHIN. PHYS. LETT. Vol. 32, No. 6 (2015) 067502

Magnetization Reversal Process of Single Crystal α-Fe Containing a Nonmagnetic Particle

LI Yi(李翼)[1,3], XU Ben(徐贲)[1], HU Shen-Yang(胡深洋)[2], LI Yu-Lan(李玉兰)[2], LI Qiu-Lin(李丘林)[1,3], LIU Wei(刘伟)[1,3**]

[1]*School of Material Science and Engineering, Tsinghua University, Beijing 100084*
[2]*Pacific Northwest National Laboratory, Richland 99352, USA*
[3]*Graduate School at Shenzhen, Tsinghua University, Shenzhen 518055*

(Received 12 January 2015)

The magnetization reversal process and hysteresis loops in a single crystal α-iron with nonmagnetic particles are simulated in this work based on the Landau–Lifshitz–Gilbert equation. The evolutions of the magnetic domain morphology are studied, and our analyses show that the magnetization reversal process is affected by the interaction between the moving domain wall and the existing nonmagnetic particles. This interaction strongly depends on the size of the particles, and it is found that particles with a particular size contribute the most to magnetic hardening.

PACS: 75.78.Cd, 75.60.Ej, 75.60.Ch, 75.30.Hx, 75.50.Bb DOI: 10.1088/0256-307X/32/6/067502

Precipitation induced degradation of structural materials is an important issue concerning the safe operation of nuclear reactors. Under thermal and irradiation condition, the structural materials undergo embrittlement due to the precipitation of solute element rich phases or clusters. In fission reactors, irradiation assisted diffusion promotes the formation of high density nano-sized Cu-rich clusters, which is the main cause of ductile-brittle transition temperature (DBTT) increase of reactor pressure vessel (RPV) steels.[1−3] As for the fourth generation fission reactors and fusion reactors, Fe-Cr alloys, the primary candidate structure materials, suffer from embrittlement in the temperature range of 300–550℃ due to the thermal- and irradiation-induced phase separation from the solid solution phase into an Fe-rich phase and a Cr-rich phase.[4−6] Reactor-component-like RPV is irreplaceable during its service life, thus it is of great meaning to monitor the embrittlement situation online and nondestructively.

Measurements of magnetic property change can be a good candidate method for non-destructive monitoring of the microstructure change of irradiated structural materials. It was shown that, with the neutron fluence increasing in RPV steels, the magnetic coercivity appears to increase due to the precipitate of Cu-rich particles.[7,8] In irradiated or thermal aged Fe-Cr steels, a good linear correlation between magnetic coercivity and micro Vickers hardness was revealed and both of them are resulted from the precipitates.[9,10] Permeability[11] and magnetic Barkhausen noise (MBN),[12,13] information stemmed from the hysteresis loop measurement, were also used to investigate the material response after irradiation. These results indicate that magnetic technology could be a promising nondestructive evaluation (NDE) tool to monitor the structural components embrittlement induced by nonmagnetic precipitates.

The experimental results mentioned above are somewhat encouraging. However the mechanism of magnetic hardening induced by nonmagnetic precipitations is poorly understood, which reduces the reliability of using magnetic property change for nondestructive evaluation of degradation of nuclear structure materials. The motivation of this work is to study the effect of irradiation defects such as nonmagnetic particles on the magnetization reversal process and to improve the fundamental understanding of NDE for nuclear structural material degradation.

A model system of single crystal α-Fe with nonmagnetic particles is simulated. The nonmagnetic particles could be Cu or Cr precipitates, voids or carbides. For simulating a hysteresis loop, the average magnetization is calculated at each applied magnetic field. The magnetization of a grid is obtained by solving the Landau–Lifshitz–Gilbert (LLG) equation[14−16]

$$(1+\alpha^2)\frac{\partial \boldsymbol{M}}{\partial t} = -\gamma_0 \boldsymbol{M}\times\boldsymbol{H}_{\rm eff} - \frac{\gamma_0\alpha}{M_{\rm s}}\boldsymbol{M}\times(\boldsymbol{M}\times\boldsymbol{H}_{\rm eff}), \quad (1)$$

where $\boldsymbol{M}$ is the magnetization vector, $M_{\rm s}$ is the saturation magnetization of the magnetic phase, γ_0 is the gyromagnetic ratio, α is the dimensionless damping constant, and $\boldsymbol{H}_{\rm eff}$ is the effective magnetic field. The LLG equation is solved numerically by a fractional step procedure of the Gauss–Seidel approach and fast Fourier transform.[15,16]

A simulation cell volume of $256\,\text{nm}\times 1024\,\text{nm}\times 1\,\text{nm}$ ($x = 256\,\text{nm}$, $y = 1024\,\text{nm}$, $z = 1\,\text{nm}$) with the size of a grid of $1\,\text{nm}\times 1\,\text{nm}\times 1\,\text{nm}$ is adopted in our simulations, and periodic boundary conditions (PBC) are applied in the x-, y-, and z-directions. A two-dimensional (2D) model is used due to the concern of computation time. A magnetic field is applied along the x-direction. The maximum applied magnetic field ($H_{\rm max}$) is $30\,\text{kAm}^{-1}$, and the increment or decrement

**Corresponding author. Email: liuw@mail.tsinghua.edu.cn
© 2015 Chinese Physical Society and IOP Publishing Ltd

of the applied field is $0.1\,\mathrm{kAm^{-1}}$. The corresponding material constants used in the simulation are as follows: $M_\mathrm{s} = 1.71 \times 10^6\,\mathrm{Am^{-1}}$, $\gamma_0 M_\mathrm{s} = 0.385 \times 10^9\,\mathrm{s^{-1}}$ and $\alpha = 0.05$. The energy coefficients of the cubic anisotropy are $K_1 = 4.80 \times 10^4\,\mathrm{J{\cdot}m^{-3}}$ and $K_2 = 5.0 \times 10^3\,\mathrm{J{\cdot}m^{-3}}$. The exchange stiffness constant is $A_\mathrm{c} = 1.5 \times 10^{-11}\,\mathrm{J{\cdot}m^{-1}}$.

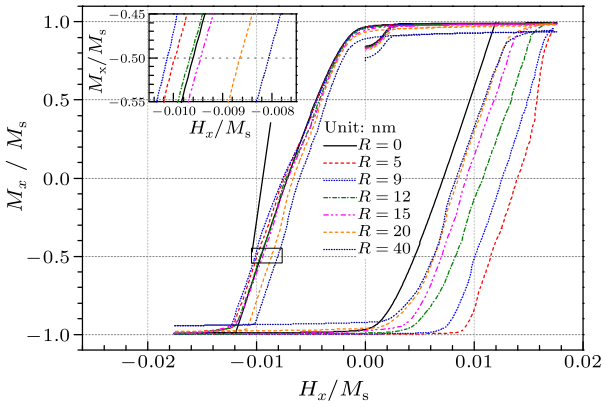

Fig. 1. Hysteresis loops for the simulated volume of $256\,\mathrm{nm} \times 1024\,\mathrm{nm} \times 1\,\mathrm{nm}$ containing a nonmagnetic particle. The radii of the particles are $R = 0$ (no particle inside), 5, 9, 12, 15, 20 and 40 nm, respectively. The inset shows the magnified figure of the rectangle area.

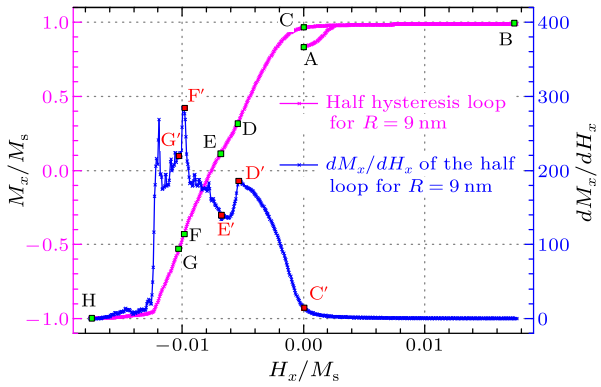

Fig. 2. Half hysteresis loop and plot of dM_x/dH_x versus H_x for the simulated volume of $256\,\mathrm{nm} \times 1024\,\mathrm{nm} \times 1\,\mathrm{nm}$ with a 9-nm-radius nonmagnetic particle inside.

The nonmagnetic particles are assumed to be of a cylinder shape of radius R. The hysteresis loops for the cases of $R = 0$, 5, 9, 12, 15, 20 and 40 nm are plotted in Fig. 1. It is seen that the hysteresis loops are asymmetric with respect to the applied field due to the fact that the magnetization reversal processes for the left and right half branches are different. In this study, we focus on the left half branch which reveals the interaction between the moving domain wall and the existing nonmagnetic particle. The case with a particle of $R = 9\,\mathrm{nm}$ is used as an example to illustrate this interaction. The left half branch of the hysteresis loop and dM_x/dH_x versus H_x are plotted in Fig. 2, where dM_x/dH_x is the derivative of the magnetization component (M_x) with respect to the applied field (H_x) and it is used to characterize the change rate of magnetization. Some critical points are marked by A–H in Fig. 2, and the corresponding domain morphologies of these points are displayed in Fig. 3. The domain morphology is illustrated by the arrow plot of the magnetization vector on the x–y plane. The black arrows are the magnified magnetic vectors of the local regions. The color represents the magnitude of the M_z component (the magnetization in the z-direction) as depicted by the color bar.

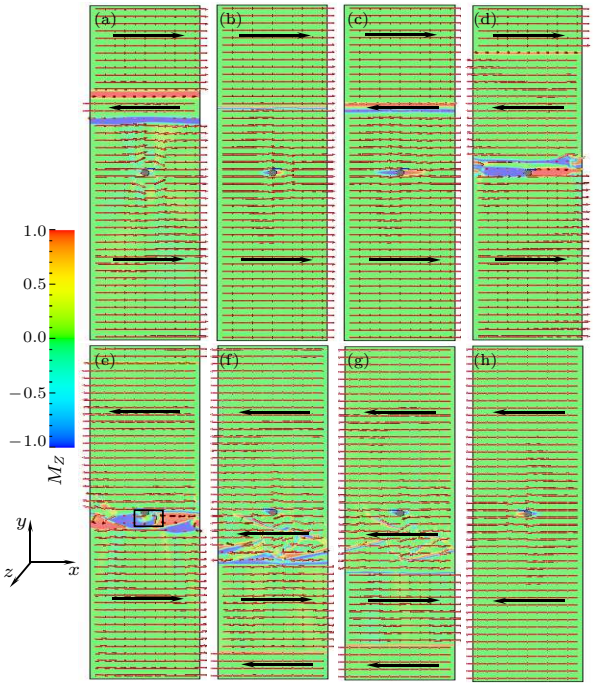

Fig. 3. The domain morphologies of points (a)–(h) in Fig. 2 for the simulated volume of $256\,\mathrm{nm} \times 1024\,\mathrm{nm} \times 1\,\mathrm{nm}$ with a 9-nm-radius nonmagnetic particle inside.

Figure 3(a) shows the initial domain morphology consisting of one nonmagnetic particle in the central and two opposite-direction 180° domain walls (DWs) in the simulation cell. As the applied magnetic field increases from zero and reaches H_max in the positive x-direction ($+H_\mathrm{max}$), the two 180° DWs come together and form a 360° DW[17,18] in Fig. 3(b). Around the nonmagnetic particle there are two subsidiary spike domains[19] where the magnetization vectors are perpendicular to the x–y plane. As the applied field decreases to 0 from $+H_\mathrm{max}$, the magnetization reversal process starts by splitting the 360° DWs into two opposite-direction 180° DWs, between which there is a reversed domain of $(-M_\mathrm{s},\ 0,\ 0)$, as illustrated in Fig. 3(c). At the same time, the spike domains extend along the x-direction. As the applied magnetic field reverses its direction to the negative x-direction and increases its magnitude to the magnetic field at point D in Fig. 2, the two 180° DWs move oppositely at an increasing rate (see Fig. 2). After that, as the applied magnetic field continues to increase its magnitude in the negative x-direction, dM_x/dH_x drops down from point D′, as shown in Fig. 2. Comparing Fig. 3(e) with Fig. 3(d), it is found that, when the red 180° DW is kept on moving, the blue 180° DW

will be pinned by the particle through its surrounding spike domains. At the same time the spike domains slowly grow wider and larger. The pinning of the DW retards the magnetization reversal process. Another feature demonstrated in Fig. 3(e) is that the magnetization of some area in the spike domains beside the particle, as shown by the marked rectangle, turns its direction to the negative x from the positive z-direction. This indicates that the nonmagnetic particle in the spike domains can be a nucleation site of reversed domain. When the applied magnetic field increases from its value at point E to that of point F, the nucleation and growth of this new formed reversed domain resume the magnetization reversal process, as demonstrated from the increasing dM_x/dH_x in Fig. 2. When almost all the spike domains switch their magnetization to the negative x-direction, the original 90° DW between the spike domains and the domain with magnetization along the positive x-direction becomes a new 180° DW (see Fig. 3(g)). This new formed 180° DW moves forward to accomplish the magnetization reversal process.

From the above analysis we find the asymmetric hysteresis loops in Fig. 1 due to the fact that the mechanism of the magnetization reversal process is different from the left to the right branch. For the left branch of the hysteresis loop from $+H_{\max}$ to $-H_{\max}$, the reversed domain nucleates at the 360° DW (see Fig. 3(c)) when the applied magnetic field decreases to 0, the DW of the reversed domain encounters and interacts with the nonmagnetic particle, which causes DW pinning as analyzed above. At $-H_{\max}$, the DWs annihilate as displayed in Fig. 3(h). Thus the nonmagnetic particle becomes a nucleation site of the reversed domain during domain switching when the applied field varies from $-H_{\max}$ to $+H_{\max}$. During such a reversal process, larger particles make it easier for a reversed domain to nucleate and grow, thus the corresponding coercive field is smaller. This nucleation-type magnetization reversal process has been analyzed in Ref. [16].

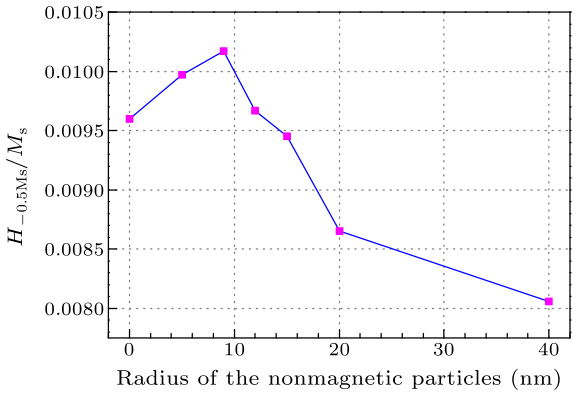

Fig. 4. $H_{-0.5M_s}$ versus the radius of the nonmagnetic particle, where $H_{-0.5M_s}$ is the applied field at $M_x = -0.5M_s$ and is used to evaluate the magnetic hardening effect.

It is found from the hysteresis loops and domain morphologies that the influence of a nonmagnetic particle on the magnetization reversal process has been lost when M_x reaches $-0.5M_s$ for all the studied cases. Thus the magnitude of the magnetic field at $M_x = -0.5M_s$ ($H_{-0.5M_s}$) is resulted from dM_x/dH_x variation and is used to evaluate the magnetic hardening effect of nonmagnetic particles in current work.

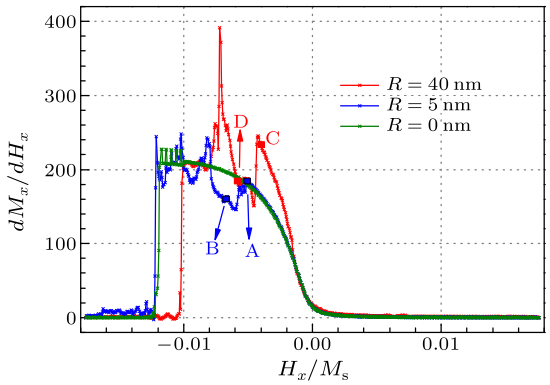

Fig. 5. Plot of dM_x/dH_x versus H_x for simulated volume of 256 nm × 1024 nm × 1 nm with nonmagnetic particles of radii $R = 0$ (no particle), 5 and 40 nm respectively.

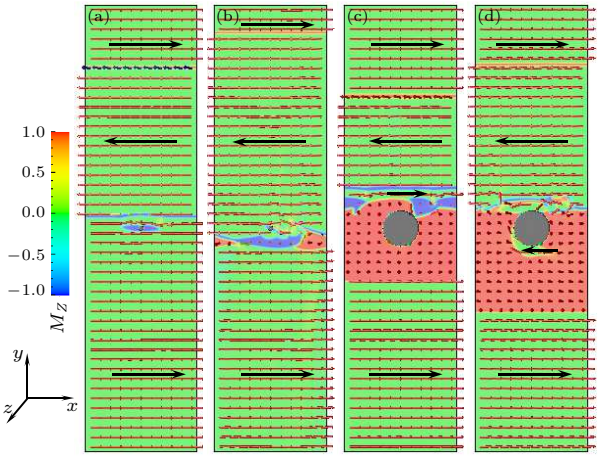

Fig. 6. The domain morphologies of points A, B, C and D in Fig. 5. Points A and B are for the case with a nonmagnetic particle of radius $R = 5$ nm, and points C and D are for the case with a nonmagnetic particle of radius $R = 40$ nm.

We obtain $H_{-0.5M_s}$ of all the studied cases and plot them versus the particle size in Fig. 4. It can be seen that $H_{-0.5M_s}$ increases with the particle size, reaches its maximum and then decreases. The reason for this tendency is illustrated in Figs. 5 and 6, in which the cases for particles of radii $R = 5$ nm and $R = 40$ nm are provided as examples. The variation of dM_x/dH_x versus H_x for the two cases are shown in Fig. 5 and the domain morphologies of points A, B, C and D on the curves of Fig. 5 are displayed in Fig. 6. The dM_x/dH_x curve for the case of $R = 0$ is also plotted in Fig. 5 for comparison. For the case with the particle of $R = 5$ nm, the spike domains around the particle are so small that the 180° DW passes through the particle without strong hindrance, which is demonstrated in Figs. 6(a) and 6(b). Figure 5 also reveals that the

decline of dM_x/dH_x is limited as compared with the case of $R = 9$ nm in Fig. 2, thus the magnetic hardening is less prominent. For the case of $R = 40$ nm, the spike domains grow fast before encountering the 180° DW, which causes a larger value of dM_x/dH_x in Fig. 5. When the 180° DW reaches the spike domains, it is hindered by the spike domains and thus causes a drastic decrease of dM_x/dH_x. At the same time, however the other side of the spike domains is kept on propagating and a new reversed domain nucleates in the spike domains, which resumes the magnetization reversal process immediately and increases dM_x/dH_x (see Figs. 5 and 6(d)). Actually, the average dM_x/dH_x is larger than the case without any particle by comparing the dM_x/dH_x curves of $R = 0$ and $R = 40$ nm. Thus the corresponding $H_{-0.5M_s}$ is smaller than the case without any particle.

It must be mentioned that the deduction of Fe content can reduce the maximum magnetization ($M_{\max}$), while its effect on the magnetic hardening effect is very limited in the current work. We can see phenomenology from Fig. 1 that $H_{-0.5M_s}$ is resulted from the change of $M_{\max}$ and dM_x/dH_x, and if dM_x/dH_x is the same as the case of $R = 0$, then a small amount of deduction of $M_{\max}$ would reduce $H_{-0.5M_s}$ by nearly the same proportion. The deduction of $M_{\max}$ contributed by Fe content decrease is very limited as compared with the change of $H_{-0.5M_s}$, thus its effect on magnetic hardening effects is ignored in this work. Obviously the magnetic hardening effect is due to the dM_x/dH_x variation which is caused by the interaction between the DW and nonmagnetic particle.

In summary, we have investigated the effect of nonmagnetic particles on the magnetization reversal process based on the LLG equation. The nonmagnetic particle is normally attached by subsidiary spike domains which can hinder the movement of the DW and thus retard the magnetization reversal process. On the other hand, the nonmagnetic particle can be a nucleation site for reversed domain, whose growth can promote the magnetization reversal process. Based on the analysis of the domain morphologies and hysteresis loops, the magnetic hardening effect of nonmagnetic particles is evaluated, and the results show that the magnetic hardening effect is of the most prominent at a particular size of the particle. For smaller particles, the associated spike domains are too small to cause a large magnetic hardening effect. For particles with an oversize, however, the easy nucleation and growth of the new reversed domain around the nonmagnetic particle in the spike domains decrease magnetic hardening effects. These results are helpful to improve the fundamental understanding of magnetic hardening behind the observed experiments and to develop NDE technology for structural materials degradation in nuclear reactors.

References

[1] Lucas G E 2010 *J. Nucl. Mater.* **407** 59
[2] Miller M K and Russell K F 2007 *J. Nucl. Mater.* **371** 145
[3] Nagai Y, Takadate K, Tang Z, Ohkubo H, Sunaga H, Takizawa H and Hasegawa M 2003 *Phys. Rev.* B **67** 224202
[4] Matijasevic M and Almazouzi A 2008 *J. Nucl. Mater.* **377** 147
[5] Konobeev Y V, Dvoriashin A M, Porollo S I and Garner F A 2006 *J. Nucl. Mater.* **355** 124
[6] Porollo S I, Dvoriashin A M, Vorobyev A N and Konobeev Y V 1998 *J. Nucl. Mater.* **256** 247
[7] Kempf R A, Sacanell J, Milano J, Guerra M éndez N, Winkler E, Butera A, Troiani H, Saleta M E, Fortis A M et al 2014 *J. Nucl. Mater.* **445** 57
[8] Barroso P S, Horváth M and Horváth Á 2010 *Nucl. Eng. Des.* **240** 722
[9] Mohapatra J N, Kamada Y, Kikuchi H, Kobayashi S, Echigoya J, Park D G and Cheong Y M 2011 *J. Phys.: Conf. Ser.* **266** 012041
[10] Mohapatra J N, Kamada Y, Kikuchi H, Kobayashi S, Echigoya J, Park D G and Cheong Y M 2011 *IEEE Trans. Magn.* **47** 4356
[11] Vandenbossche L, Konstantinović M J and Dupré L 2008 *J. Magn. Magn. Mater.* **320** e562
[12] Park D G, Park S S, Ju J S, Chang K O and Hong J H 2004 *J. Magn. Magn. Mater.* **272** 1512
[13] Park D G, Park I G, Kim W W, Cheong Y M and Hong J H 2008 *Nucl. Eng. Des.* **238** 814
[14] Gilbert T L 2004 *IEEE Trans. Magn.* **40** 3443
[15] Zhang J X and Chen L Q 2005 *Acta Mater.* **53** 2845
[16] Hu S Y, Li Y L, McCloy J, Montgomery R and Henager Jr C 2013 *IEEE Magn. Lett.* **4** 3500104
[17] Jang Y, Bowden S R, Mascaro M, Unguris J and Ross C A 2012 *Appl. Phys. Lett.* **100** 062407
[18] Dean J, Kohn, A, Kovacs A, Zeltser A, Carey M J, Hrkac G, Allwood D A and Schrefl T 2011 *J. Appl. Phys.* **110** 073901
[19] Cullity B D and Graham C D 2009 *Introduction to Magnetic Materials* 2nd edn (Birlin: Wiley-IEEE Press) p 306